Analysis of an adverse pressure gradient turbulent boundary layer with 2D- and 3D-time-resolved particle tracking

Matthew Bross[1][*], Thomas Fuchs[1], Christian J. Kähler[1]

[1] Universität der Bundeswehr München,
Institute of Fluid Mechanics and Aerodynamics, Neubiberg, Germany

[*] matthew.bross@unibw.de

Abstract

Time-resolved planer and tomographic flow fields extending from the near-wall region to log-layer of a turbulent boundary layer subjected to an adverse pressure gradient (APG) are examined at $Re_\tau = 5000$. In order to characterize the near- and far-field interaction, a thin planer field of view, extending from the viscous to the log-layer was measured with a time-resolved 2D particle tracking method. The three-dimensional flow dynamics close to the wall were resolved by measuring a volume in the viscous sublayer region with a novel high resolution tomographic particle tracking technique. It is shown that this technique is able to fully resolve mean and time dependent features of the complex three-dimensional flow with accurately down to very near-wall distances (<1 viscous unit). The time record of the turbulent flow is used to create space-time correlations that demonstrate the footprint of the far field on the near-wall region. Furthermore, from time-resolved Lagrangian particle trajectories, statistical information as well as instantaneous topological features of near-wall flow events are deduced. In particular, rare localized separation events are shown to appear in relatively organized groupings in both spanwise and streamwise directions. Moreover, reverse flow events appearing in long time sequences appear associated with the motion of low-momentum streaks in the near-wall region if the surrounding fluid is also sufficiently decelerated by low-momentum flow in the log-layer. However, these types events appear relatively infrequently and remain for the most part below 10 viscous units.

1   Introduction

The behavior of turbulent boundary layers with pressure gradients is directly related to the aerodynamic performance of many technical devices. For this reason the physical understanding of these types of flows is of great scientific and technological interest and importance. While the turbulent flows along a flat plate with zero pressure gradients were investigated in great detail in the last decades, as seen in the extensive review by Wallace (2012), however, the effect of a pressure gradient is by far less understood. Moreover, the details of the transition from the fully attached to the partly and fully separated flow states is widely unknown (Michael and Rainer, 2002; Skåre and Krogstad, 1994).

Experimental measurements of APG turbulent boundary layers in Monty et al. (2011); Knopp et al. (2015); Harun et al. (2013) study the influence of the pressure gradient on large scale structures and momentum transport as well as parametric parameter variation for the development of scaling models. However, strong agreement between various experimental and numerical databases about scaling framework is absent. Recently, Maciel et al. (2018) established a framework for the outer scaling of APG turbulent boundary layers based on various experimental and numerical databases, but due to the lack of high quality near wall data at large Reynolds numbers, they mention that the derived framework for scaling and governing parameters is not complete.

Of particular interest for the present investigation are relatively rare instances of small localized reverse flow events because they might be the nucleus for the generation of macroscopic flow separation in adverse pressure gradient boundary layers. In recent years, the numerical prediction of reverse flow events in channel (Lenaers et al., 2012) and turbulent boundary layer flows (Spalart and Coleman, 1997) has achieved strong attention. As the spatial extent of these events is very small according to Cardesa et al. (2014), and

their occurrence extremely seldom (Lenaers et al., 2012), their detection in experiments was quite challenging. However, in recent years their existence could be confirmed experimentally by using long-range micro PTV (Buchmann et al., 2016), long-range micro PIV (Willert, 2015; Willert et al., 2018) and micro pillars (Brücker, 2015) techniques. In addition, a very recent computational investigation of flow over an airfoil with increasing pressure gradient (Clauser pressure parameter $\beta = (\delta^*/\tau_o)\partial p/\partial x$ = 0.6 to 35) was performed by Vinuesa et al. (2017). They concluded that back flow events are much more probable for increasing APG conditions, reaching probabilities of up to 30% for extremely strong APGs. In addition, wall shear stress fluctuations were analyzed in a DNS investigation of a zero pressure gradient turbulent boundary layer at Re_τ up to 680 by Diaz-Daniel et al. (2017). This computation also showed that for increasing Reynolds number an increase in negative wall shear events. It was also established that a strong correlation between reverse flow events and strong spanwise flow exists and they further provided evidence that these events may be related to quasi-streamewise oriented vortices in the near-wall region.

The aforementioned numerical and experimental studies were performed mostly at relatively low Reynolds numbers ($Re_\tau <$ 2500) and mostly zero pressure gradients. The probability of such events occurring was measured to be around 0.01% (Willert, 2015), 0.012-0.018% (Willert et al., 2018),and 0.06% (Lenaers et al., 2012) in DNS channel flow, which makes statistical analysis of reverse flow events difficult. Furthermore, the experimental investigations only yield information about the footprint of the reverse flow events on the wall shear stress (Brücker, 2015) and the characteristics of the structures in an arbitrary slice selected by the light-sheet used for the planar PIV and PTV investigation by Buchmann et al. (2016) and Willert (2015). However, recent technological progress in image acquisition and quantitative flow visualization allows for the possibility of fully three-dimensional time-resolved velocity measurements (Novara et al., 2016; Kähler et al., 2016; Fuchs et al., 2016; Schanz et al., 2016). Moreover, the quality of the PTV measurements techniques has reached a high level, as shown in this investigation, such that flow effects in the viscous sublayer of a turbulent boundary layer can be examined experimentally, even at larger Reynolds numbers.

The motivation for measuring in the near-wall region is to resolve the three-dimensional near-wall cycle which is connected to coherent large scale motion in logarithmic region of the turbulent boundary layer (Lenaers et al., 2012). This connection allows for the manipulation of these reverse flow events by means of macroscopic flow control methods. This may be beneficial for delaying flow separation (by reducing the number of reverse flow events) or by decreasing the viscous drag of fully attached flows (by increasing the appearance of reverse flow events). It is possible that the reverse flow events are associated with the interaction of near-wall low-speed streaks Kline et al. (1967); Smith and Metzler (1983) and low-momentum superstructures Buchmann et al. (2016) but, this has not been demonstrated experimentally or numerically so far.

In the investigation presented herein, the topology and statistics of near-wall reverse events will be discussed and their connection with both the flow in the wall-normal and spanwise directions. Since the volumetric measurement is limited to the near-wall region an additional planer measurement that extends from the near-wall region to the log-region was preformed. As these reverse flow events appear very seldom in low Reynolds number turbulent boundary layers along flat plates with zero pressure gradient we examine these structures and under the effect of an adverse pressure gradient to make a statistical analysis of the rare reverse flow events possible. Furthermore, it will also be possible to examine their scale and dynamics and if the events appear randomly in space and time or in packets with a characteristic frequency. To resolve the spatial and temporal details of the near-wall flow with high accuracy and spatial resolution, a novel tomographic tracking technique was developed to record time-resolved flow fields in the viscous sublayer. Furthermore, information about the flow in the spanwise direction is now available from the results presented herein, which is absent from previous two-dimensional PIV studies.

2 Experimental Systems and Methods

Turbulent boundary layer experiments were performed at the Universität der Bundeswehr München in the Atmospheric Wind tunnel Munich (AWM). The Eiffel type wind tunnel has a 22 m long test section with a cross section of approximetly 2×2 m^2 and flow velocities up to 40 m/s can be achieved. A 7 m long polished aluminum boundary layer model consisting of two S-shaped deflections on either end of a 4 m flat plate zero pressure gradient (ZPG) section, was installed along the side wall of the wind tunnel. The adverse pressure gradient (APG) region (downstream of the ZPG part starting at X = 5.75 and ending at X = 7 m, with a initial boundary layer thickness of 180 mm for Re_τ = 5000) was fitted with a glass viewing window of size 0.26×0.59 m^2, see figure 1. The X-direction indicates the streamwise distance along the wind tunnel, starting at the beginning of the model. Global boundary layer parameters, including β and $\partial p/\partial x^+$, were

measured in Reuther et al. (2015) for the same boundary layer model and Reynolds number and are reported in table 1.

Table 1: Boundary layer parameters

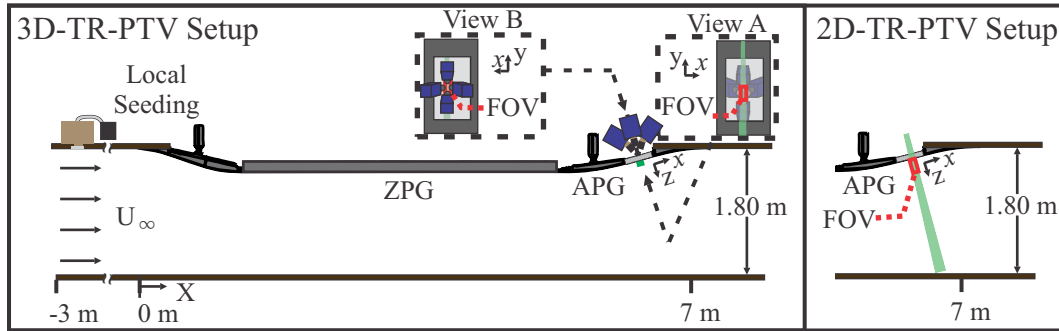| Parameter			3D-TR-PTV	2D-TR-PTV
measurement location	X	[m]	6.25	6.30
free stream velocity	U_∞	[m s^{-1}]	10	9.8
BL thickness	δ_{99}	[m]	0.197	0.201
displacement thick.	δ^*	[m]	0.0383	0.0435
momentum thick.	θ	[m]	0.0230	0.0257
pressure gradient	$\partial p/\partial x$	[Pa m^{-1}]	33.6	35.1
	$\partial p/\partial x^+$		0.035	0.040
friction velocity	u_τ	[m s^{-1}]	0.191	0.186
wall unit	ν/u_τ	[μm]	81	83
friction Re	Re_τ		5000	5000
wall shear rate	$\partial u/\partial z|_{z=0}$	[s^{-1}]	4300	4340

Figure 1: Plan view of boundary layer model in AWM and 3D- and 2D-TR-PTV setup.

In order to perform quantitative flow visualization, a local seeding system was installed upstream of the boundary layer wall, providing uniform seeding with a high tracer particle concentration near the wall. This local seeding system is located approximately 2 m before the aluminum model to avoid contamination of the wind tunnel screens by large amounts of seeding produced by a global seeder, as a contamination can lead to unwanted disturbances of the flow (Bradshaw, 1964, 1965). The local seeding system was constructed by covering a 50×1000 mm^2 slit in the wind tunnel wall with a large wooden box. On the inside of the tunnel, the slit was covered with an aluminum plate, with a regular arrangement of 2 mm circular holes, mounted flush to the side wall. The wooden box was connected to a conventional impactor seeding generator that creates DEHS particles with an approximately 1 μm mean diameter, (Kähler et al., 2002). The box was filled with tracer particles, which are sucked through the aluminum grid into the boundary layer due to the reduced pressure in wind tunnel. This system is ideal for boundary layer experiments, as the seeding is fed directly into flow region of interest. Furthermore, the location and concentration of the tracer particles can be easily varied by adjusting the position and number of openings in the aluminum plate and the settings of the seeding generator. The disturbance to the flow is minimal as the particles are sucked out of the reservoir by means of the slightly lower pressure in the wind tunnel test section. Moreover, a homogeneous concentration of particles could be reached at the measurement location because of the natural turbulent mixing of the particles inside the boundary layer along the model.

The tracer particles in the APG region were illuminated in a wall-normal plane and thin wall-parallel volume for the 2D and 3D configurations respectively (see figure 1) by a continuous wave laser (Kvant Laser) with maximum output power of 8 W and 532 μm wavelength. For the volumetric measurement, the laser beam was formed into a uniform sheet of 40 mm width and thickness of about 1 mm and aligned directly adjacent to the wall. This beam profile was determined by using DataRay Inc. WinCamD-LCM1C beam profiling camera.

Time-resolved particle image sequences for the planer wall-normal PTV measurements were captured

with 1 high-speed CMOS camera with 36GB of RAM (Dimax-S4, PCO GmbH, LaVision) mounted on top of the wind tunnel to view the laser sheet perpendicularly, see figure 1. Using 100 mm/f2.8 Zeiss objective with a 2x tele-conversion lens, the resulting resolution in the center of the FOV was $\sim$26 μm/pix. By dividing the pixel pitch of the HS camera (11 μm/pix) the resulting magnification in the center of the FOV was $M = 0.42$, corresponding to a field of view of 7.5×30.3 mm^2.

The 3D time-resolved PTV measurement were captured with 4 high-speed CMOS cameras (Dimax-S4, PCO GmbH,LaVision) mounted in a 30° cross configuration behind the glass viewing window in the APG, see figure 1. The coordinate system (x, y, z) defined in View A corresponds to the streamwise, spanwise, and wall-normal directions respectively. Using 50 mm/f2.8 Zeiss objectives and Scheimpflug mounts, the resulting resolution in the center of the FOV was $\sim$25 μm/pix. However, the resolution of the measurement is actually better as the particle images can be located with sub-pixel resolution (Kähler et al., 2012a,b). By dividing the pixel pitch of the HS camera (11 μm/pix) the resulting magnification in the center of the FOV was $M = 0.44$, corresponding to a field of view of $17 \times 25 \times 0.8$ mm^3. The boundary layer thickness, determined from previous large field measurements at the measurement location, was $\delta_{99} \approx 190$ mm. An overview of the imaging parameters is given in table 2.

Table 2: Imaging parameters for PTV

Parameter			3D-TR-PTV	2D-TR-PTV
recording rate	f	[Hz]	8200	7500
exposure time		[μs]	24	20
resolution	m	[μm/pix]	25	26
magnification	M		0.44	0.42
field of view, FOV (3D)	x, y, z	[mm^3]	$17 \times 25 \times 0.8$	
	x, y, z	[$(\nu/u_\tau)^3$]	$200 \times 294 \times 9.5$	
field of view, FOV (2D)	x, z	[mm^2]		7.5×30.3
	x, z	[$(\nu/u_\tau)^2$]		90×365
image sequence.			$2 \times 55\,000$	$2 \times 55\,000$
particle image per pixel	N_{ppp}		0.022	0.002

The evaluation of the data was performed with a in-house tomographic reconstruction method (Fuchs et al., 2016, 2017) and time-resolved particle tracking (based on Cierpka et al. (2013a)) algorithms. For the 2D imaging, a volume reconstruction was not necessary, instead the 2D locations of the particle images were identified using a Gaussian peak detection algorithm and then tracked using the aforementioned time-resolved methods. In contrast to PIV, particle tracking greatly enhances the spatial resolution as spatial averaging over an interrogation window is avoided (Kähler et al., 2012a,b). Since near-wall flows typically feature very strong spatial gradients, especially when small vortices create reverse flow events, particle tracking is a well suited measurement technique. However, reliable particle identification can be difficult for high seeding concentrations especially when the mean particle distance is much smaller than the mean displacements. Since modern high-speed cameras allow for the time-resolved sampling of the tracer particles, the temporal information can be used to enhance the reliability and accuracy of the tracking procedure (Cierpka et al., 2013a; Kähler et al., 2016; Schanz et al., 2016).

Each found particle trajectory is then unambiguously identified by its common identification number and the algorithm estimates the velocity for each trajectory (particle positions in three-dimensions and time) separately. The velocity estimation is based on a second order polynomial fit of four consecutive positions. Taking the integral of the polynomial curve allows for a correction of the velocity estimation and to compensate bias errors due to curvature effects (Scharnowski and Kähler, 2012). In addition, the vector position is reallocated and placed directly on the polynomial curve instead of in between the two positions as typically done in two-frame representations. This method is especially suited for the correct estimation of the velocity and vector position for trajectories with strong curvature (Cierpka et al., 2013a) as typically for the reverse flow events in the near-wall region of turbulent boundary layers (Bross and Kähler, 2016; Schröder et al., 2016). However, if only two or three successive positions are known (i.e., end of a trajectory or short trajectories), the velocity estimation is based on the classical first order displacement estimation and second order vector positioning (Wereley and Meinhart, 2001).

3 Trajectory Length and Validation

The length of particle trajectories can be quite different depending on their speed and where or when they enter or exit the measurement volume. With the aforementioned tracking method, many of the particle images reconstructed in the volume were assigned to trajectory IDs, i.e. all particle images in one trajectory are assigned a unique identifier. More specifically, 7000 (on average) particle images in the reconstructed volume were assigned to a trajectory of minimum length 1, i.e. track length = 1 means that two successive images of the same particle are connected and the displacement between these particle images is calculated.

In order to understand the distribution of trajectory lengths, an ideal rectangular measurement volume with a uniform light intensity distribution can be considered, according to figure 2. It can be expected that the longest possible continuous tracks of length d, like Track A, appear if a particle enters the volume at the beginning of the image acquisition and disappears at the end of the volume during the image sequence. If the measurement time is sufficiently long, then the longest tracks are associated with particles that move close to the wall with a low velocity. Therefore, it follows that the faster the particles' motion, the shorter the track length will be. Trajectories consisting of only a few particle images can occur when a particle enters the measurement domain at the end of the recording sequence or if a particle is inside the measurement domain at the beginning of the image acquisition, see trajectories labeled B in figure 2.
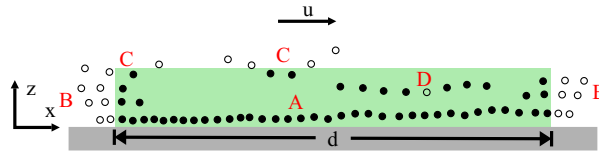

Figure 2: Ideal laser sheet and trajectories

Short trajectories are more likely to appear at the boundaries of the measurement volume when particles associated with a longer trajectory briefly enter the light sheet and are detected, see particles labeled C. In the present case, the probability of detecting short particle paths at the boundaries will increase because of the thin extent of the volume in wall-normal direction and the turbulent nature of the flow under investigation. Moreover, another cause of short trajectories occurs when two particles images overlap in the measurement volume. This will cause a matching disparity during the volume reconstruction which will break longer tracks into separate tracks of smaller length, as shown by track D. This effect can occur quite often because of the relatively dense seeding concentration inside the measurement volume. Considering the previous discussion, it is reasonable to use the track length as a detection criteria to remove valid but short particle tracks from the flow analysis.

4 Mean Field

In order to determine the proper inner scaling, the friction velocity, u_τ, has to be estimated from the slope of the mean velocity profile at the wall. The mean velocity profile was computed by sorting the trajectories into equally spaced bins in the z-direction and extending over the xy-planes. For the mean flow results, bins of z-direction spacing 25μm and 12.5 μm were used for the 2D and 3D measurements respectively. This bin spacing was selected so that sufficient data points appear within each bin.

The position of the wall is also important for the proper inner scaling and wall shear rate calculations, $\partial u/\partial z|_{z=0}$. In the 2D measurement the orientation of the camera and the light sheet allows for the visualization of both the particle image and their reflection on the glass viewing window. The wall position is then calculated by applying the parallax correction method outlined in (Cierpka et al., 2013b) for each particle-mirror image pair. For the 3D measurement, the wall position is directly determined from the original camera calibration. For this experimental configuration a dual plane calibration target is placed directly on the window, which results in the $z = 0$ location of the reconstructed volume being at the wall position. This calibration procedure is only possible when the wind tunnel is not operating. Therefore, to account for any small shift in the wall position due to the negative pressure difference between the inside and outside of the test section, the wall position can be confirmed in two other ways. First, the distribution of the reconstructed particle images in the z-direction clearly shows any shift in the wall location. Furthermore, a linear fit of the mean streamwise velocity profile will give a z-intercept corresponding to the correct wall position.

Comparing the aforementioned methods it made it possible to determine, with relative certainty, that the wall shifted a constant 0.05 mm during in all experiments presented herein.

Moreover, at the far-edges of the measurement volume, the number of particles imaged will be limited due intensity profile of the laser. In these regions, the low number of particle images may have a strong effect on the statistical quantities because outliers in this region can significantly alter the mean value and must be rejected. To account for this, a continuous distribution (Gauss fit) of the particle images in each bin. With this fit applied, the mean field in each bin can be calculated by either taking the peak of the Gauss fit or taking the mean of values within 2σ. For this investigation, velocities within 2σ of the fit applied to each bin were used to create the mean field and corresponding Reynolds Stress plots shown in figures 3(a) and 3(b) respectively.
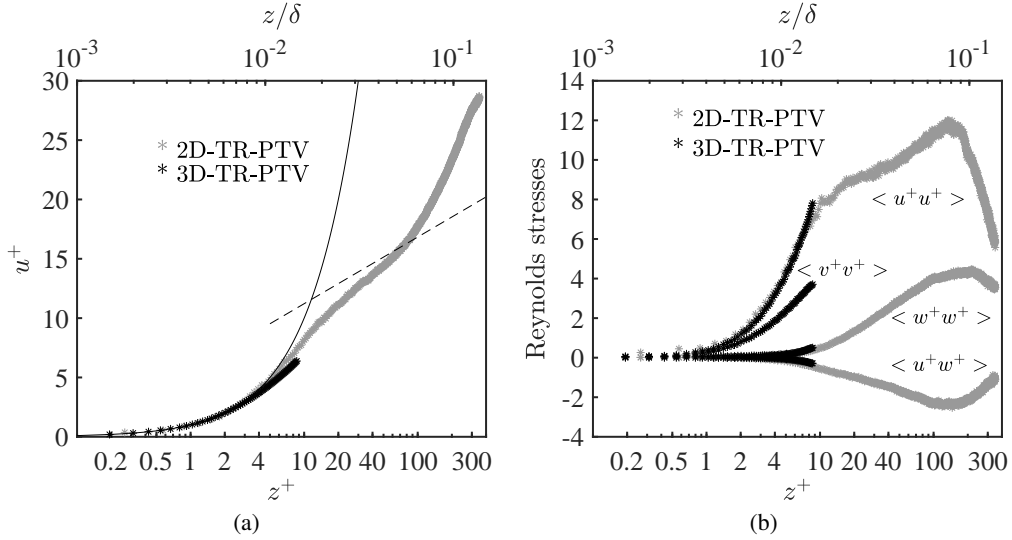

Figure 3: (a) Mean streamwise velocity field and (b) Reynolds Stresses in viscous and outer scaling in APG at $Re_\tau = 5000$

Very good agreement between the 2D and 3D data sets for both the mean velocity and Reynolds stresses is seen in figures 3(a) and 3(b). Only for $z^+ > 8$ the 3D results are slightly biased towards smaller velocities. This can be explained by several points, first the large displacements at the edge of the volume reduce the detection probability. Second, the slightly elongated particle images in this faster moving region increase the reconstruction uncertainty in this region. In the forgoing sections, most of the analysis involving the 3D data only considers the regions where $z^+ < 8$.

For this data set it appears that correct mean values were achieved for between $0.1 < z^+ < 8$ and $0.2 < z^+ < 310$ for the 3D and 2D sets respectively. The standard deviation of the mean values velocity values was estimated to be no larger 0.05 m/s. Due to having reliable data points in the linear region ($z^+ = u^+$) of the turbulent boundary layer flow, calculating the viscous scaling is straight forward. A linear fit of $\bar{u}$ vs. $\bar{z}$ in the region $1 < z^+ < 5$, where $u = \bar{u}+u'$ and $\bar{z}$ is the average bin position in the z-direction, allows for the calculation of $u_\tau = \sqrt{\nu d\bar{u}/d\bar{z}|_{z=0}}$ and the z-intercept indicates the wall location. Therefore, $u^+ = \bar{u}/u_\tau$ and $z^+ = z \cdot u_\tau/\nu$ can directly be calculated. The friction velocity was found to be, $u_\tau = 0.191$ m/s and, which corresponds to a viscous length of $\nu/u_\tau = 81$ μm for the 3D data set. Correspondingly, for the 2D data set, $u_\tau = 0.186$ m/s and $\nu/u_\tau = 83$ μm. The slight differences in these values for 2D and 3D sets can be explained by the slightly different streamwise measurement locations, see table 1. The standard deviation of the velocity and displacement for both data sets was estimated to be (in viscous units) 0.3 and 0.1 respectively.

5   Flow field correlations

Using the time information in the recorded data, it is possible to make correlations in both space and time. Space-time correlations have played an important role in the statistical analysis of temporal and spatial scales in turbulence flows, see Wallace (2014) and references therein. In the following section space-time correlations are calculated directly from 2D time resolved data set using the following generalized form,

$$R_{d_i d_j}(\vec{x}, \vec{r}, t) = \frac{\langle d_i(\vec{x}, t_o) d_j(\vec{x} + \vec{r}, t_0 + t) \rangle}{\sigma_{d_i(\vec{x}, t_o)} \sigma_{d_j(\vec{x} + \vec{r}, t_0 + t)}} \tag{1}$$

Where d_i and d_j ($i, j = 1,2$) are fluctuations such as velocity or wall shear stress, τ_w. The vector, $\vec{x} = (x, z)$ is a point at a specific location in the streamwise and wall normal directions that is then shifted in the wall normal direction by $\vec{r} = (x, z + \Delta z)$ and by incremental time steps $t_o + t$. In other words the correlation is calculated by selecting a position and time series (x, z, t_o) and correlating that series for all other wall normal locations and shifted in time by t.

In the following correlation plots the vertical and horizontal axis are scaled in both inner and outer normalization, i.e. $z^+ = z u_\tau / \nu$, z/δ, $t^+ = t u_\tau^2 / \nu$, and $t U_f / \delta$. Furthermore, the correlation calculation is made by averaging sub-samples of the entire record time sequence, the latter being approximately $t U_f / \delta = 300$ or $t^+ = 13000$ for each time record. The correlation in figures 4 and 5(a) are calculated for sub-sets of 1400 images corresponding to $t^+ = \pm 100$ or $t U_f / \delta = \pm 2.32$. For figure 5(b) the time shift is $t^+ = \pm 25$ or $t U_f / \delta = \pm 0.61$.

To begin this analysis, the auto-correlation of the streamwise velocity u at a starting point near the outer peak ($\sim z/\delta = 0.065$) is shown in figure 4. In this plot a strong positive correlation with almost no time shift within the log-layer is visible. However, as the buffer and viscous layers are approached, the correlation shifts in the forward time direction. In contours plotted, R_{uu} values between 0.2-0.3 persist down to the wall and are shifted by around $t^+ = 25$ or $t U_f / \delta = 0.6$. Although the correlation is relatively small, the footprint of the far field in the near wall region is evident.
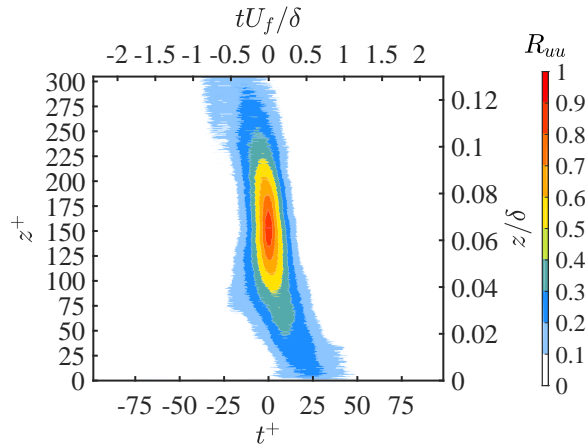

Figure 4: Space time correlation, R_{uu} from starting point at the outer-peak ($\sim z/\delta = 0.065$)

Looking closer at the behavior near the wall, the wall shear stress τ_w is correlated with u in figure 5(a). In this case, a positive correlation is shown in the wall normal direction but skewed in the negative time direction. The strong correlations of the wall shear stress and u end around the buffer layer but similarly to figure 4 there is a weak correlation value extending into the log layer and outer peak region.
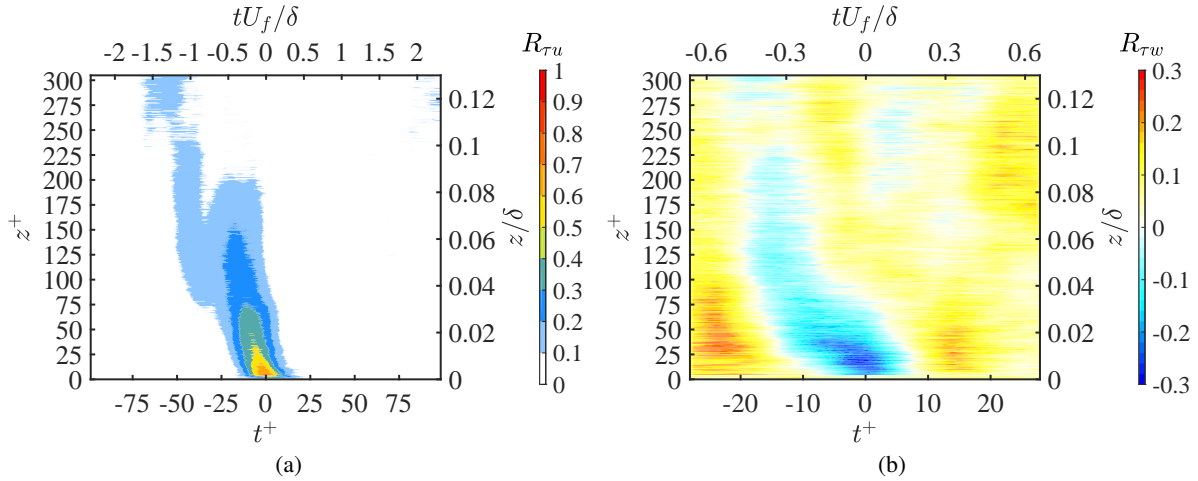
Figure 5: Space time correlation, (a) $R_{\tau_w u}$ (b)$R_{\tau_w w}$.

Finally, with the readily available wall normal velocity w, the correlation of the wall shear stress and w is also calculated and is shown in the figure 5(b). In this plot a strong positive or negative correlation was not found as was shown in figures 4 and 4. However, a negative correlation of between = -0.1 and -0.3 with negative time shift extend from the wall to the log-layer. The maximum negative correlation appears at ($-0.85t^+$,$17z^+$). Likewise, regions of equally small positive correlation are found on either side of the negative correlated region.

6 Space-time Visualization

In this section the interaction between the near- and far-field flow features over a long time series is asesed. Furthermore, localized seperation events that appear within this time series are also highlihted. In figure 6 freestream fluctuation fields from the wall to the log-region are plotted over a long time sequence. This representation is usufull in relating relatively rare events, e.g. localized seperation, to more commen features of the flow such as elongated superstructures and near-wall streaks. This plot was made by selecting a thin wall normal slice of the flow field and plot all the trajectories passing through that slice with time. In the case of the wall-normal planer data, trajectories passing through a thin (streamwise) strip extending from the wall to 350 viscous units over 45000 image sequences, corresponding to $t^+ = 12500$ or $tU_f/\delta = 290$, is plotted in figure 6. The trajectories are colored with the streamwise fluctuating velocity, u', scaled with the local wall-normal mean velocity, $\bar{u}$. A similar plotting approach was used for ZPG turbulent boundary layers in Willert (2015).

The first things immediately visible in figure 6 are the intermittent regions of low- ($u'/\bar{u} < 0$) and high- ($u'/\bar{u} > 0$) momentum regions. Since this data is compressed in order to show a long time sequence, the these regions in the log-layer are actually elongated structures in space. Interesting, often these regions go all the way down to the wall, which indicates that a low or high momentum structure is aligned with a corresponding low or high speed near-wall streak. Sometimes the regions only exist for tU_f/δ = 1-2 and other times there are sustained low or high momentum regions that persist for more that tU_f/δ = 10. A few examples of these short and sustained regions of low- and high-momentum are indicated in respective dashed boxes in figure 6.

Also plotted in figure 6 are regions of reverse flow in purple where $u < 0$. The relatively sparse temporal distribution of the reverse flow events allows for the detection of such events by visual inspection. Upon this inspection it can be concluded that reverse flow regions appear relatively infrequently (around 1%). In many cases the reverse flow events only exist for a short amount of time ($< 50t^+$) and remain close to the wall ($z^+ < 10$), e.g. at 1000-1500t^+ and 4050-9700t^+. If the probability of reverse flow is calculated for each wall-normal location, almost 90% of them occur below $z^+ = 10$ as shown in figure 7. Predictably, the locations where these reverse flow events occur coincide with regions of low momentum, as the flow must be sufficiently decelerated so that the flow reversal can happen.
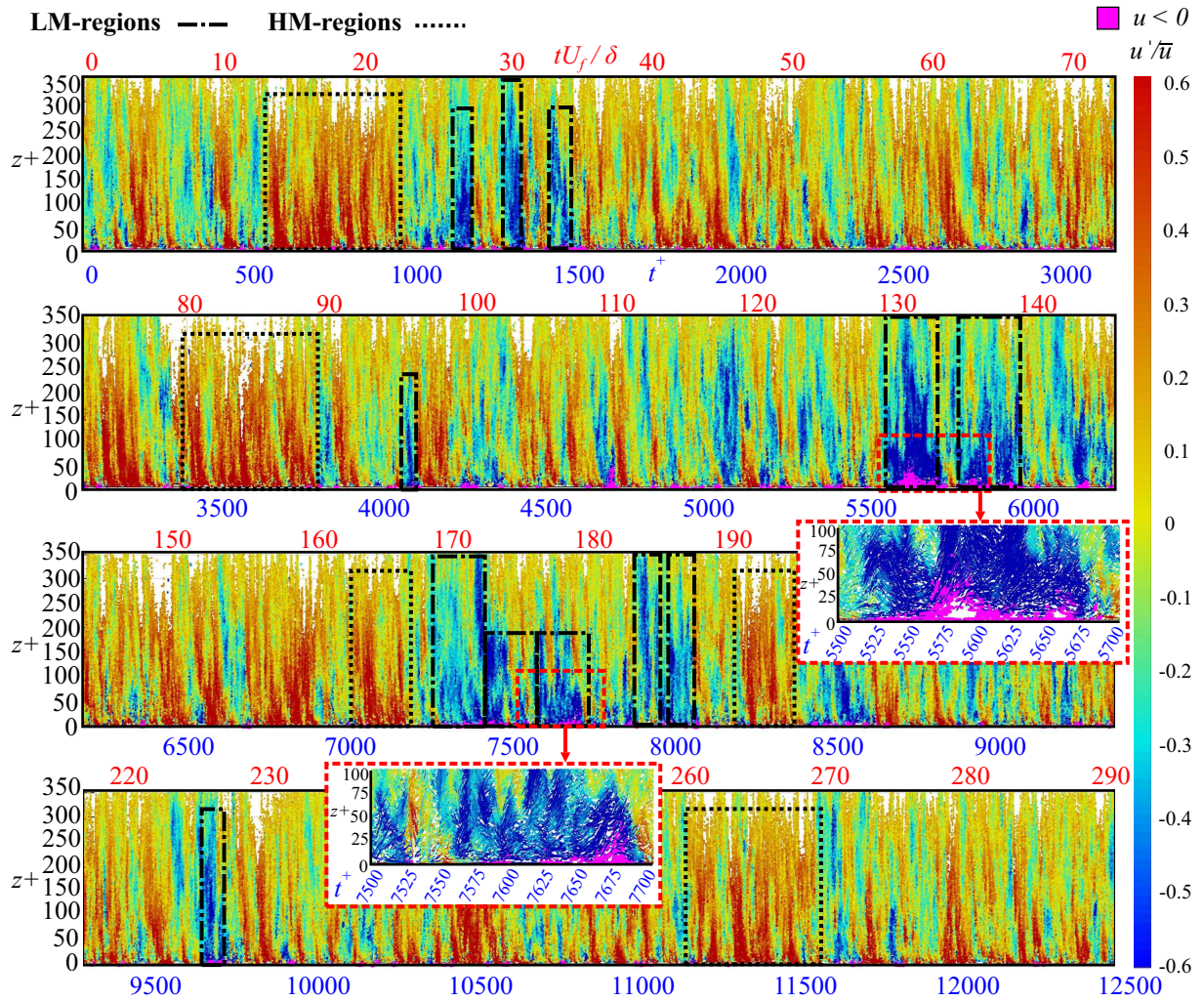
Figure 6: Space-time plot over $t^+ = 12500$ or $tU_f/\delta = 290$, from the 2D data set colored with $u'/\bar{u}$ and purple regions represent $u < 0$. Selected high-momentum (HM) and low-momentum (LM) regions are indicated in dashed boxes.
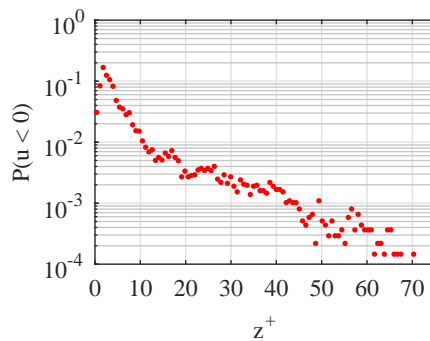

Figure 7: Probability of reverse flow $u < 0$ vs z^+.

However, there are instances where a large or extreme reverse flow events appear that persist for more than $150t^+$ or $4\text{-}5tU_f/\delta$ and extend past $z^+ = 50$, e.g. 5500-5700t^+ and 7500-7700t^+. These improbable (according figure 7) events are shown in a zoomed in view in figure 6. In these cases, a large decelerated region appears in the surrounding flow field and extends well into the buffer and log-layer. The lifetime and spatial distribution of these decelerated flow regions can be explained by the superposition of elongated low-momentum superstructure on a low-speed near-wall streak. Further evidence of this superstructure and streak layering is evidenced by the large regions of accelerated flow, e.g. 13-23tU_f/δ and 79-89tU_f/δ, which can be explained by the superposition of high-momentum superstructures on high-speed near-wall streaks. Therefore, it appears, based on figure 6, that under this superimposed condition large or extreme reverse events can take place.

What is absent from the figure 6 is information about the flow in the spanwise direction (y-direction). In the following discussion, near-wall features and distribution of reverse flow events in the spanwise direction and how they are associated with the meandering near-wall streaks will be shown. As this information is embedded in the 3D near-wall data set a corresponding space-time plot was made. In this case, trajectories passing through a wall-normal ($z^+ = 1\text{-}5$) and spanwise (310 y^+) volume over a sub-set of the entire data set (20000 image sequences or 4450t^+ or 98tU_f/δ) is plotted in figure 8. The trajectories are colored with the streamwise fluctuating velocity,u', scaled with the local wall-normal mean velocity, $\bar{u}$. Reverse flow is indicated in purple where $u < 0$.
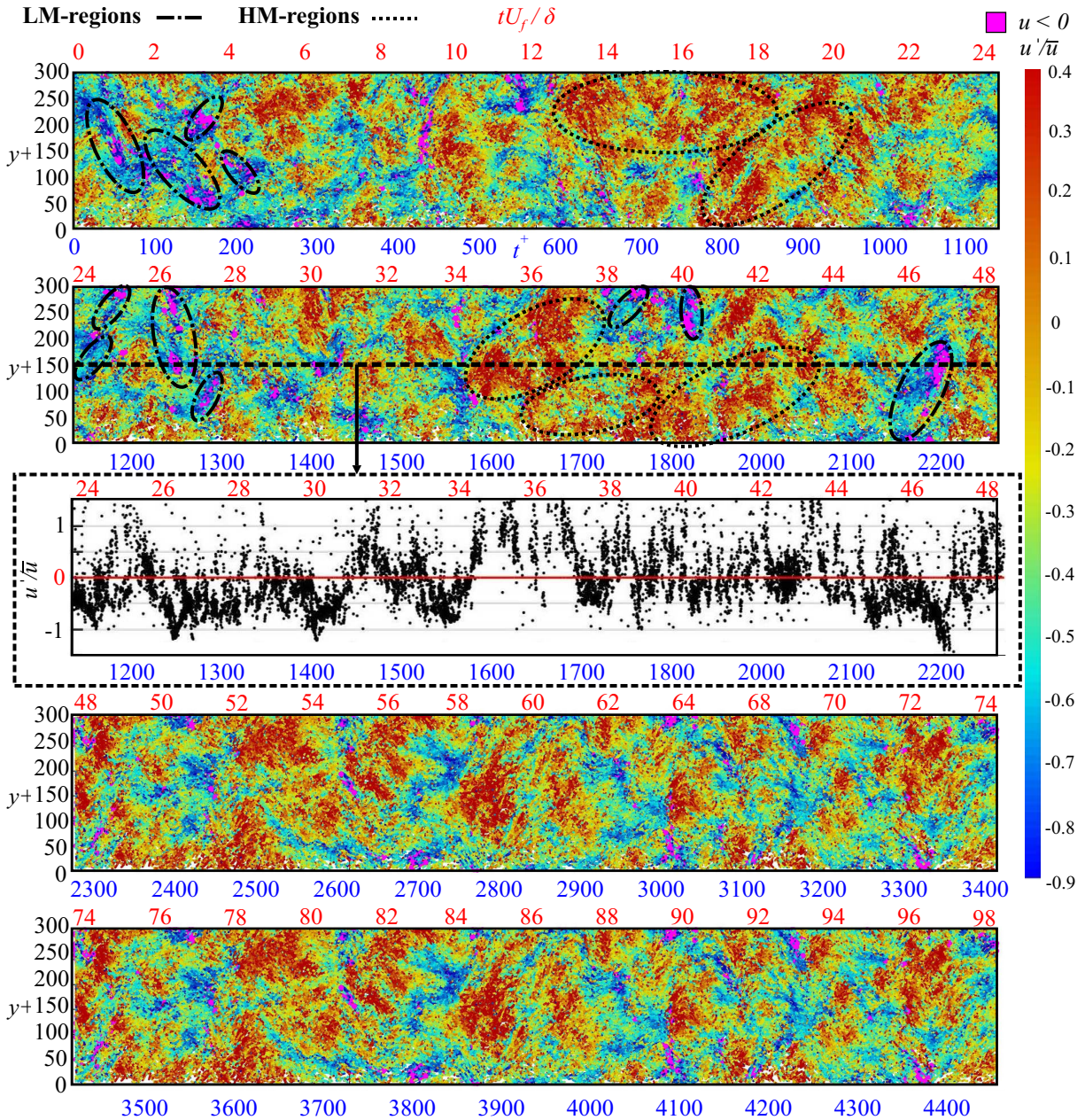
Figure 8: Space-time plot over $t^+ = 4450$ or $tU_f/\delta = 98$, from the 3D data set colored with $u'/\bar{u}$ and purple regions represent $u < 0$. Selected high-momentum (HM) and low-momentum (LM) regions are indicated in dashed boxes.

What is immediately visible in this plot is the low- and high- speed near-wall streaks and the locations of reverse flow events with respect to the streaky pattern. It appears that in almost all the cases shown here that the reverse flow events occur inside or at the edge of a low-speed streak, a few of which are indicated in dashed ellipses in figure 8. Furthermore, it appears that when a reverse flow event appears in a low-speed streak, that low-speed streak is often strongly tilted in the spanwise direction. This indicates the presence of streamwise oriented vortices that when slightly tilted, induce a slight flow reversal.

As observed in figure 6, in the near-wall topology there are sometimes regions of fast moving streaks that persist for 200-$300 t^+$ or 6-$8 t U_f/\delta$ (indicated in dashed ellipses). This can also be seen in the line plot

of $u'/\bar{u}$ for a cut through the data at $y^+ = 150$. Although only the viscous sublayer is visualized there, this extended region of fast moving streaks is consistent with the lifetime of the superposition of superstructure and streaks shown in figure 6.

What is also visible is the appearance of groupings for reverse flow events, distributed in the spanwise direction, e.g. between $0\text{-}250t^+$ and $1150\text{-}1300t^+$. As established in figure 6, in order for these groupings to occur, the flow in the near-wall and far field regions must be sufficiently decelerated. This can be achieved, if a low-momentum superstructure is superimposed on a near-wall low-speed streak. In other words, groupings of reverse flow events can occur only when the flow is sufficiently decelerated by the layering of low-speed near-wall streak and a elongated low-momentum superstructure in the far field. A statistical analysis of these topological and dynamic features is provided in the next section.

7 Statistics of Reverse Flow Events

7.1 Reverse Flow Detection

In the following sections a statistical analysis of the reverse flow events is presented in order to quantitatively characterize their occurrence frequency, connection with other extreme events, and preferred orientation in the spanwise direction. Furthermore, only statistics from the near-wall three-dimensional data set are accessed.

The probability of reverse flow based on the distribution of instantaneous streamwise velocity is shown in figure 9(a). In this plot the maximum probability occurs at a $u^+ = 1.5$ and rather sharply decreases for values less than zero. In this case the probability of reverse flow, calculated by summing the region for $u^+ < 0$ or $\tau_w < 0$ in figure 9(a), is relatively low, 0.01 or 1%. This value represents a much larger value than presented in other measurements for ZPG boundary layer and channel flow (Willert et al., 2018; Willert, 2015; Lenaers et al., 2012). However, in the DNS channel flow computation in Lenaers et al. (2012), an increase in reverse flow probability for increasing Re_τ up to 1000 was reported. Furthermore, an increase in reverse flow probability was also reported for increasing APG conditions in Vinuesa et al. (2017), which is intuitive, as more flow reversal is expected as separation is approached. Therefore, the relatively large reverse flow measured herein at $Re_\tau = 5000$ for a turbulent boundary layer with APG conditions is in accordance with the trends reported in the aforementioned DNS studies.

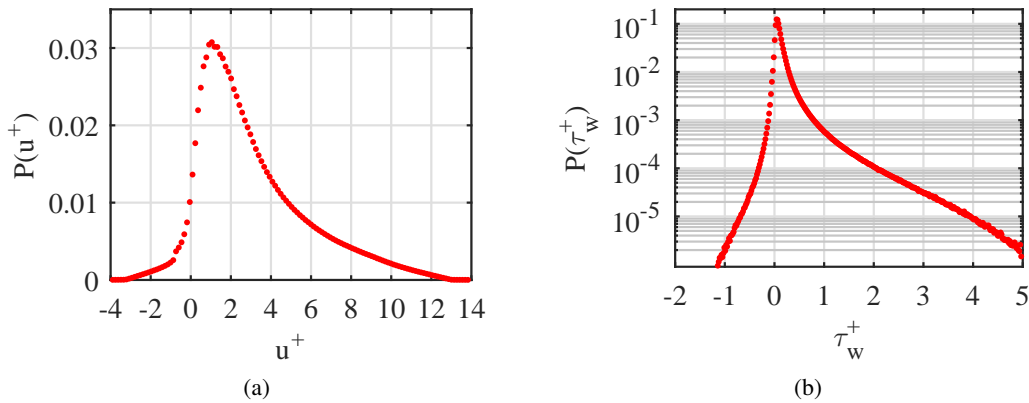(a)   (b)

Figure 9: (a) Inner scaled instantaneous streamwise velocity and (b) Inner scaled instantaneous wall shear stress PDFs, from 3D-TR-PTV fields.

The low probability of reverse flow can also be illustrated by calculating the instantaneous wall shear stress. Taking advantage of the high spatial resolution in the viscous sublayer, the wall shear stress, $\tau_w = \mu \partial u / \partial z|_{z=0}$, can be directly calculated. The probability distribution function for inner scaled wall shear stress is provided in figure 9(b).

In the aforementioned discussion and figures the probability of individual reverse flow vectors was considered. However, it must be kept in mind that a reverse flow event is comprised of many reverse flow vectors and therefore the occurrence probability of reverse flow event is actually much smaller, as will be discussed in section 7.4.

7.2   Reverse Flow and Extreme Wall-Normal Events.

Another potentially interesting feature of the near-wall region are wall-normal events. These events which may be associated with the sweep (Q4) and ejection (Q2) of the near-wall streaks have been well documented and discussed in the literature (see review Wallace (2012)). In this section, the connection of extreme wall-normal fluctuations and the reverse flow will be explored in order to determine if there is a link between them. In figure 10(a) the probability density function of the instantaneous wall-normal velocity, w, normalized with the w_{rms} is shown. In this plot, the probability of fluctuations beyond $\pm 8 w_{rms}$ is several orders of magnitude lower then maximum and therefore events outside of this range will be referred to as extreme events.

To examine the connection of wall-normal fluctuations and reverse flow evetns a JPDF of u/u_{rms} and w/w_{rms} is plotted in 10(b). In this figure it appears that there is not a strong correlation between extreme wall-normal events (beyond $\pm 8 w_{rms}$ and reverse flow events $u/u_{rms} < 0$, which is in agreement with DNS results at lower Reynolds number Lenaers et al. (2012); Vinuesa et al. (2017). This shows that reverse flow events are a feature of the flow that are not connected to extreme wall-normal events.
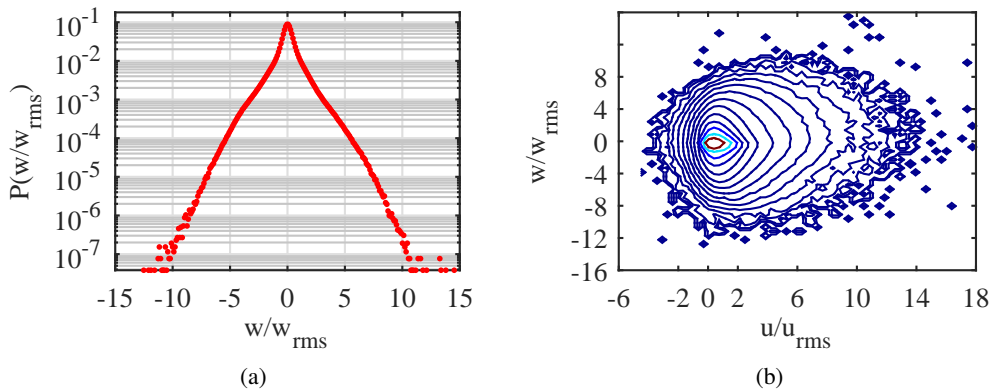

(a)   (b)

Figure 10: (a) Wall-normal fluctuations PDF and (b) JPDF of wall-normal and streamwise fluctuations

7.3   Flow Direction Statistics

In the previous analysis showed the characteristics of reverse flow events, i.e. their size, extent in the wall normal direction and dynamics. Furthermore, it was shown that reverse flow events are not connected with extreme wall normal events. Therefore, in this following section the orientation of reverse flow events is analyzed. Specifically their connection to spanwise motion of the near wall streaks, which could already be seen qualitatively in figure 8. To examine if there is a connection between reverse flow events and strong spanwise motion, the flow direction based on the u and v vector components (the wall-normal velocity component is of little effect when compared to the other components) is calculated. In order to separate more extreme events the data set is conditioned into two groups with $|\tau_w| > \tau_{w,rms}$ and $|\tau_w| < \tau_{w,rms}$. The probability at each angle for each conditioned set is provided in 11. In these plots, $0°$ and $360°$ degrees indicate flow in the positive x-direction and $180°$ is flow purely in the negative x-direction. For each case the flow direction with the lowest probability was used to normalize the rest of the probabilities and then is scaled logarithmically. It must be noted that the conditioning requirement, $|\tau_w| > \tau_{w,rms}$, reduces the data set to only 35% of the original set. Nonetheless, the preferred flow direction of these more intense events will provide insight into the larger turbulent action of the flow in the near-wall region.

(a)   (b)
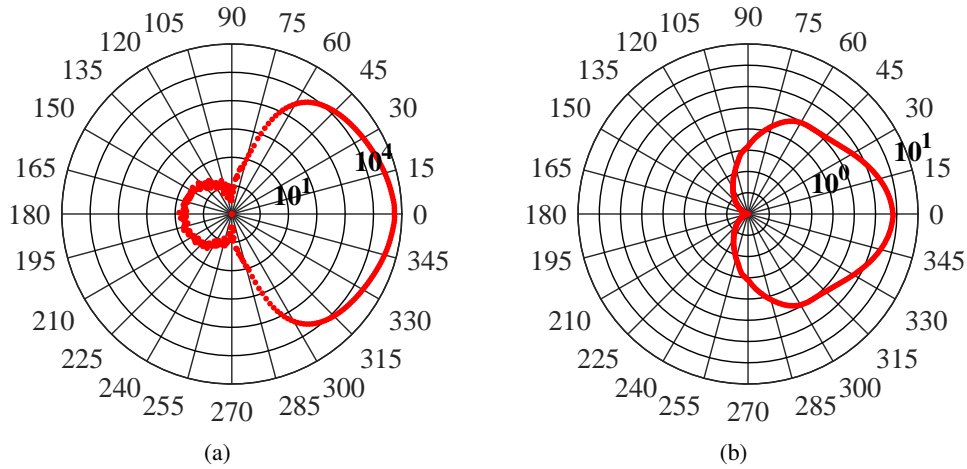
Figure 11: Logarithmically scaled flow direction probabilities for (a) $|\tau_w| > \tau_{w,rms}$ and (b) $|\tau_w| < \tau_{w,rms}$

In figure 11(a), where $|\tau_w| > \tau_{w,rms}$, the flow directions with the lowest probability occur at 90° and 270°, see figure 11(a). Relative to the probability at 90° and 270°, the flow is almost two orders of magnitude more likely to travel in the 180° direction. Therefore, it seems for these more intense fluctuations, the flow direction is most likely to have a streamwise orientation during a reverse flow event. This was also seen in the the DNS study for strong APG conditions in Vinuesa et al. (2017). However, when looking at the other conditioned set of $|\tau_w| < \tau_{w,rms}$, which represents a much larger portion of the data set, a different distribution is present. In figure 11(b), the least likely probability occurs at 180° and the reverse flow for these fluctuations are more likely to have a strong spanwise component.

7.4   Reverse Flow Event Lifetime

In the preceding sections, efforts to qualify the experimental data and analyze statistical properties of individual velocity vectors have been made. However, there must be a distinction made between an individual reverse flow vector and a reverse flow event. Furthermore, in both figure 6 and 8 it was shown that sometimes flow reversal appears in groups. The distinction is made more evident by visualizing how the vectors with negative streamwise velocity are grouped throughout a time series. Therefore, in figure 12 vectors with $u^+ < 0$ are grouped into bins of 50 time sequences.

As demonstrated in the space time plots (figure 8), many intervals exist where almost no reverse flow events are detected. Secondly, it appears that reverse flow vectors often appear in groups. This does not necessarily mean that they interact in these groups, but it seems that once a reverse flow event is detected, it is likely to find more events within a short time period. By using analysis of this type, it is possible to locate image ranges where significant reverse flow occurs. Furthermore, if one roughly considers the probability of major reverse flow events (bins with amplitudes larger than 2000) it is one order of magnitude less than previously calculated for individual reverse flow vectors, i.e. 0.1% compared to 1%. If the events seen in the 2D data set are counted from figure 6 in this way, a similar percentage of 0.15% of reverse flow events is measured.
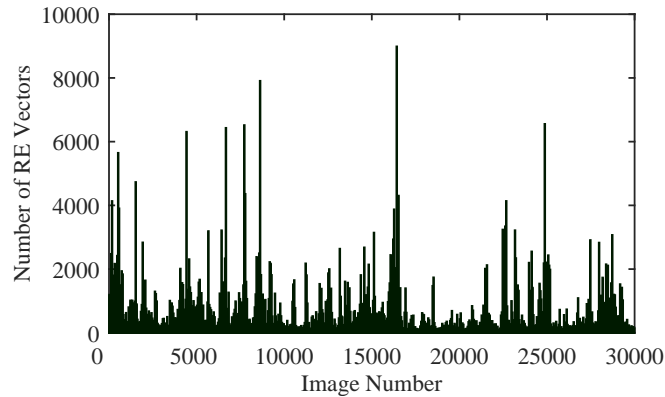
Figure 12: Reverse flow event detection over a time series, from 3D-TR-PTV fields.

The lifetime of large events is around 10 ms to 20 ms or $24t^+$ to $48t^+$ where $t^+ = (tu_\tau^2/\nu)$ but they can appear one after each other in a low speed streak for up to and beyond 100 ms (or $240t^+$).

8 Reverse Flow Event Visualization

In the following section, trajectory plots for a few of the extreme reverse flow events are provided. This is done to not only understand the topology of these events but also further show the connection between extreme reverse flow events and low-speed near-wall streak, low-momentum superstructures, and tilted longitudinal vortices.

In figure 13 a sequential set of flow trajectories during one of the large reverse flow events identified in figure 6 is shown in physical space with streamwise velocity coloring. In this case, each plot (t1,t2,...) represents particle trajectories over 100 image sequences ($28.1t^+$). Highlighted in purple are reverse flow vectors. What can be seen in this sequence is the continued deceleration of the flow in the wall-normal direction (from t1 to t3) due the presence of a low-momentum large scale structure impinging on the wall, which sufficiently decelerates the flow allowing for the large flow reverse shown in plots t4 and t5. After this sequence of course the reverse bubble remains close to the wall (in t6 and t7) while the outer flow accelerates until the flow reversal disappears in t9.
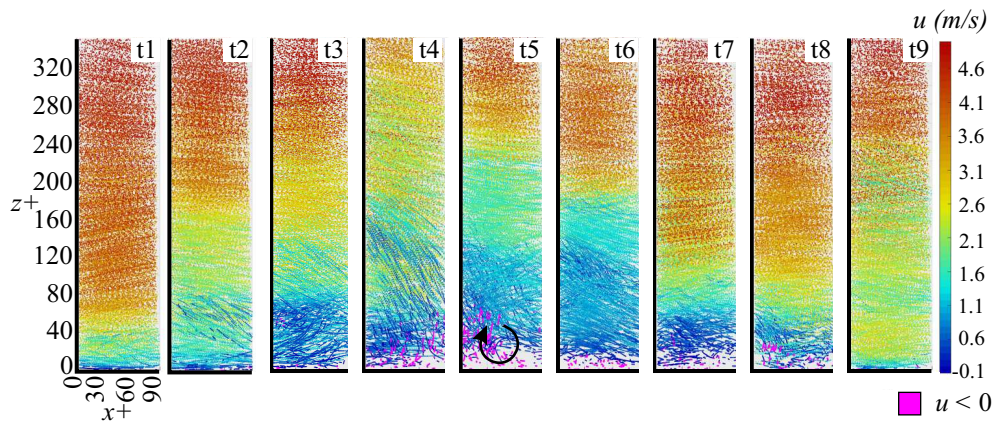

Figure 13: Trajectory plot during reverse flow event from 2D-TR-PTV data set.

Furthermore, a selection of reverse events based on the maximum amplitude of the peaks in figure 12 are

visualized in figure 14 by plotting three-dimensional trajectories colored with $u'/\bar{u}$. With this color coding, regions of low and high-momentum with respect to the mean velocity can be quantitatively determined. Reverse flow, i.e. $u < 0$, is highlighted in purple.

The left plot, (a), in figure 14 shows trajectories over a time series of 100 images ($28.4t^+$). Two views of the volume are shown, one in the x and y plane and also a view looking at the volume from the left side of the xy plot in the zy plane. For this particular case, the streaky structure of low and high-speed streaks is immediately obvious. Also visible are $u < 0$ events distributed most prominently in the regions of low-speed. Looking at the xy view, these reverse flow events events are present in a group in the low-speed streaks across the entire streamwise extent of the measurement volume or approximately 150 viscous lengths. Moreover, the long streamwise extent of the low-speed streaks explains why the reverse flow events can be observed in packages. Following the discussion about figure 8, low-speed streaks appear to be strongly related to the existence of reverse flow events in turbulent boundary layers.
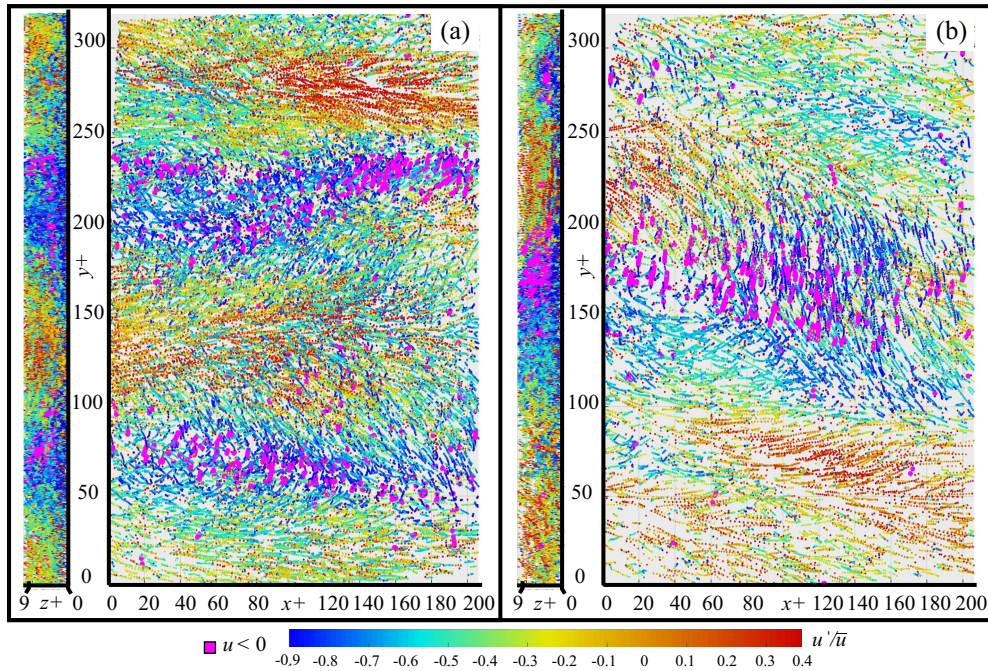

Figure 14: Three-dimensional trajectories during two different (a and b) instantaneous reverse flow events. Trajectories are colored with $u'/\bar{u}$, where positive flow is from left to right. Also highlighted are regions of $u < 0$.

To highlight difference in the topology of these reverse flow events is not universal, another set (independent of (a) of instantaneous trajectories is plotted in the right, (b), side of figure 14. In contrast to (a), the flow is dominated by one large spanwise (y-direction) directed event. Trajectories with $u < 0$ appear grouped in a defined spatial location and extend over and area of 120 by 120 viscous lengths in the streamwise and spanwise directions, which is much larger than the spanwise extent of the low speed streaks shown in (a). Furthermore, the significant spanwise motion of this flow event which was not observed to this extent in figure (a).

Considering the results presented here, it seems that the large spanwise motion must be associated with longitudinal vortices, which was previously reported in Lenaers et al. (2012); Diaz-Daniel et al. (2017). This is confirmed by the cross-plane visualization (zy view). If the axis of a streamwise vortex is slightly tilted with respect to the mean flow direction, these longitudinal vortices can generate reverse flow events, provided the vortex travels with a sufficiently low convection velocity, which is possible when the vortex is embedded inside a low-speed streak. Consequently, this generation mechanism is based on a interaction between low-speed streaks and tilted streamwise vortices. If the local convection velocity is increased locally by high-speed near-wall streaks, reverse flow events are probably suppressed and cannot appear.

9   Concluding Remarks

The work presented herein, investigates the topological features of an adverse pressure gradient turbulent boundary layer at $Re_\tau = 5000$ with a novel time-resolved tomographic PTV technique developed at the institute. This technique is able to determine with high accuracy, fine spatial resolution, and without bias errors (due to spatial averaging) the flow velocity within the viscous sublayer. Furthermore, time-resolved particle tracking measurements were performed in a single wall-normal slice in order to see both the near-wall and far field flows.

The physical characteristics of localized separation events or reverse flow events were discussed by observing space-time plots for both the 2D and 3D data sets. It was shown that the reverse events appear in a region of low-momentum extending from the wall to the log-layer. Furthermore, these types events appear relatively infrequently and remain for the most part below $z^+ = 10$. However, at least two cases were observed where large reverse flow regions occurred over many times steps that penetrate into the buffer layer. These large flow reversal regions suggest that certain relationship, e.g. superposition of low-momentum superstructure on a near-wall low-speed streak, between the near-wall flow and far field flow must exist in order to decelerate the convection velocity enough so that a relatively large event such as this can occur.

In addition, it was shown that the large events can extend in both spanwise and streamwise directions on the millimeter scale (and this case ∼100 viscous units), which is larger than the dimensions given in the literature for the ZPG case at lower Reynolds numbers. Furthermore, the relatively more frequently occuring reverse flow events measured herein under APG conditions and at relatively large Reynolds number is in agreement with the increasing trend of reverse flow probability for increasing Reynolds number and pressure gradient parameter β discussed in the DNS computations of Vinuesa et al. (2017).

In all the cases of reverse flow events measured, a region of low-momentum was observed in the surrounding area which are associated with the near-wall low-speed streaks. Furthermore, evidence of small longitudinally oriented vortices is demonstrated by the large spanwise directed trajectories in the vicinity of reverse events. The probability of the majority of reverse flow vectors having a significant spanwise component was shown to be much more likely than reverse events directed purely in the upstream direction. However for a conditioned data set where $|\tau_w| > \tau_{w,rms}$, the spanwise component of the reverse flow events was significantly diminished.

Moreover, regions of strong spanwise flow that are associated with reverse flow and $|\tau_w| < \tau_{w,rms}$ were shown to be correlated with regions of low-momentum. Which again indicates that longitudinal vortices that reside within the near-wall low-speed streaks are able to generate reverse flow events. However, these kind of reverse flow events only occur when the axis of the streamwise vortices is slightly tilted with respect to the mean flow direction, generating flow in both the spanwise and upstream (reverse) directions.

The results clearly show that reverse flow events are not necessarily unique in terms of the topology and temporal frequency and it is evident that these differences are linked with the strength of the fluctuating near-wall flow. It was also demonstrated that reverse flow events are not strongly correlated with extreme wall-normal events, which perhaps provides further insight into dynamics of the near-wall flow. However, whenever the specific conditions are reached, i.e. sufficient deceleration of the flow, multiple reverse flow events were shown to appear one after another.

It has been also demonstrated that low-speed streaks are one necessary condition for the detection of large groups of reverse flow however as low-speed streaks occur relatively frequently compared to reverse flow events, and therefore there must be additional conditions. One possible explanation could be the presence of low-momentum large-scale turbulent superstructures that are superposed on top of low-speed streaks which sufficiently reduce the momentum so that large grouping of reverse flow events can appear.

Measuring long time sequences in turbulent flows is not only useful for the statistical analysis of temporal scales but also for observing rare events that would be unlikely captured in standard double frame imaging. Double frame methods are nevertheless very useful for extracting mean statistics, the turbulent spatial scales, and two point analysis. Moreover, double or multi-frame approaches are still the only viable option for high speed flows (Buchmann et al., 2016; Giepman et al., 2015). In both the past and currently, long time sequences in wall bounded flows are often measured with hot wires (Monty et al., 2009; Mathis et al., 2009; Vallikivi et al., 2015). Although these measurements have excellent temporal resolution, the measurement location is limited to one (or several if a rake is used) wall normal location per recording. With the techniques presented herein, it is possible to extract all 3 velocity components at several wall-normal and spanwise positions simultaneously.

With the method first outlined by Willert (2015) and implemented in a similar way in the current work, it was demonstrated that by using time-resolved PIV or PTV it was possible measure the time trace of two velocities componenets at many wall normal positions simultanously. However, this uses only a thin

streamwise slice extended in the wall normal direction and in order to recover long spatial scales from the data, a mapping model must be used. Therefore, in order to test validity of these models, a simultaneous measurement of both long temporal and large spatial scales is needed. This was explored in De Kat and Ganapathisubramani (2015), where an empirical approach for mapping frequency spectra into wavenumber spectra was developed by recording a large streamwise-wall normal plane with time resolved PIV. However, wall bounded turbulence is highly three-dimensional, especially near the wall as demonstrated in the current work. Therefore, volumetric measurements are essential for properly understanding the features of the flow and their interactions. In particular, measuring time sequences in large volumes that extend from the viscous layer to past the log-layer and several boundary layer thickness in both in streamwise and spanwise directions would be useful not only to simultaneously measure both the spatial and temporal turbulent scales, but to characterize how these large meandering features interacted with the near field. Due to the large range of scales from the near-wall to the far field, demonstrating the interaction between these regions with volumetric approaches is challenging however, this is becoming obtainable as illumination, tracer particle generation, imaging, and particle tracking technologies have improved.

Acknowledgements

References

Bradshaw P (1964) Wind-tunnel screens: flow instability and its effect on aerofoil boundary layers. *J Roy Aero Soc* 68:198

Bradshaw P (1965) The effect of wind-tunnel screens on nominally two-dimensional boundary layers. *J Fluid Mech* 22:679–687

Bross M and Kähler CJ (2016) Time-Resolved 3D-PTV Analysis of Near Wall Reverse Flow Events in APG Turbulent Boundary Layers. in *18th Inter. Symp. on the App. of Laser and Imaging Tech. to Fluid Mech., July 4-7, Lisbon, Portugal*

Brücker C (2015) Evidence of rare backflow and skin-friction critical points in near-wall turbulence using micropillar imaging. *Phys of Fluids* 27:1–7

Buchmann NA, Kücükosman YC, Ehrenfried K, and Kähler CJ (2016) Wall pressure signature in compressible turbulent boundary layers. in *Progress in Wall Turbulence 2*. pages 93–102. Springer International Publishing

Cardesa JI, Monty J, Soria J, and Chong M (2014) Skin-friction critical points in wall-bounded flows. *Journal of Physics: Conference Series* 506

Cierpka C, Lütke B, and Kähler CJ (2013a) Higher order multi-frame particle tracking velocimetry. *Exp Fluids* 54:1533

Cierpka C, Scharnowski S, and Kähler CJ (2013b) Parallax correction for precise near-wall flow investigations using particle imaging. *Appl Opt* 52:2923–2931

De Kat R and Ganapathisubramani B (2015) Frequencywavenumber mapping in turbulent shear flows. *J Fluid Mech* 783:166–190

Diaz-Daniel C, Laizet S, and Vassilicos JC (2017) Wall shear stress fluctuations: Mixed scaling and their effects on velocity fluctuations in a turbulent boundary layer. *Phys of Fluids* 29:055102

Fuchs T, Hain R, and Kähler CJ (2016) Double-frame 3D-PTV using a tomographic predictor. *Exp Fluids* 57:174

Fuchs T, Hain R, and Kähler CJ (2017) Non-iterative double-frame 2d/3d particle tracking velocimetry. *Experiments in Fluids* 58:119

Giepman RHM, Schrijer FFJ, and van Oudheusden BW (2015) High-resolution piv measurements of a transitional shock wave–boundary layer interaction. *Experiments in Fluids* 56:113

Harun Z, Monty JP, Mathis R, and Marusic I (2013) Pressure gradient effects on the large-scale structure of turbulent boundary layers. *J Fluid Mech* 715:477498

Kähler CJ, Astarita T, Vlachos P, Sakakibara J, Hain R, Discetti S, La Foy R, and Cierpka C (2016) Main results of the 4th international PIV challenge. *Exp Fluids* 57:97

Kähler CJ, Sammler B, and Kompenhans J (2002) Generation and control of tracer particles for optical flow investigations in air. *Exp Fluids* 33:736

Kähler CJ, Scharnowski S, and Cierpka C (2012a) On the resolution limit of digital particle image velocimetry. *Exp Fluids* 52:1629

Kähler CJ, Scharnowski S, and Cierpka C (2012b) On the uncertainty of digital PIV and PTV near walls. *Exp Fluids* 52:1641

Kline SJ, Reynolds WC, Schraub FA, and Runstadler P (1967) The structure of turbulent boundary layers. *J Fluid Mech* 30:741–773

Knopp T, Buchmann NA, Schanz D, Eisfeld B, Cierpka C, Hain R, Schröder A, and Kähler CJ (2015) Investigation of scaling laws in a turbulent boundary layer flow with adverse pressure gradient using PIV. *J Turbulence* 16:250–272

Lenaers P, Li Q, Brethouwer G, Schlatter P, and Örlü R (2012) Rare backflow and extreme wall-normal velocity fluctuations in near-wall turbulence. *Phys of Fluids* 24:1–17

Maciel Y, Wei T, Gungor AG, and Simens MP (2018) Outer scales and parameters of adverse-pressure-gradient turbulent boundary layers.. *J Fluid Mech* 844:5–35

Mathis R, Hutchins N, and Marusic I (2009) Largescale amplitude modulation of the small scale structures in turbulent boundary layers.. *J Fluid Mech* 628:311337

Michael M and Rainer F (2002) DNS of a turbulent boundary layer with separation. *Inter J of Heat and Fluid Flow* 23:572 − 581

Monty JP, Harun Z, and Marusic I (2011) A parametric study of adverse pressure gradient turbulent boundary layers. *Inter J of Heat and Fluid Flow* 32:575–585

Monty JP, Hutchins N, NG HCH, Marusic I, and Chong MS (2009) A comparison of turbulent pipe, channel and boundary layer flows. *J Fluid Mech* 632:431442

Novara M, Schanz D, Reuther N, Kähler CJ, and Schröder A (2016) Lagrangian 3D particle tracking in high-speed flows: Shake-The-Box for multi-pulse systems. *Exp Fluids* 57:128

Reuther N, Scharnowski S, and Hain R (2015) Experimental investigation of adverse pressure gradient turbulent boundary layers by means of large-scale PIV. in *11th Inter. Symp. on PIV, September 14-16, Santa Barbara, USA*

Schanz D, Gesemann S, and Schröder A (2016) Shake-The-Box: Lagrangian particle tracking at high particle image densities. *Exp Fluids* 57:70

Scharnowski S and Kähler CJ (2012) On the effect of curved streamlines on the accuracy of PIV vector fields. *Exp Fluids* 54:1435

Schröder A, Schanz D, Geisler R, and Gesemann S (2016) Investigations of coherent structures in near-wall turbulence and large wall-shear stress events using Shake-The-Box. in *18th Inter. Symp. on the App. of Laser and Imaging Tech. to F. Mech., July 4-7, Lisbon, Portugal*

Skåre P and Krogstad P (1994) A turbulent equilibrium boundary layer near separation. *J Fluid Mech* 272:319–348

Smith CR and Metzler SP (1983) The characteristics of low-speed streaks in the near-wall region of a turbulent boundary layer. *J Fluid Mech* 129:27–54

Spalart PR and Coleman GN (1997) Numerical study of separation bubble with heat transfer. *Eurp J Mech B - Fluids* 16:169–187

Vallikivi M, Hultmark M, and Smits AJ (2015) Turbulent boundary layer statistics at very high Reynolds number. *J Fluid Mech* 779:371–389

Vinuesa R, Örlü R, and Schlatter P (2017) Characterisation of backflow events over a wing section. *J Turbulence* 18:170–185

Wallace JM (2012) Highlights from 50 years of turbulent boundary layer research. *J Turbulence* 13:1–70

Wallace JM (2014) Space-time correlations in turbulent flow: A review. *Theoretical and Applied Mechanics Letters* 4:022003

Wereley ST and Meinhart CD (2001) Second-order accurate particle image velocimetry. *Exp Fluids* 31:258–268

Willert CE (2015) High-speed particle image velocimetry for the efficient measurement of turbulence statistics. *Exp Fluids* 56:17

Willert CE, Cuvier C, Foucaut JM, Klinner J, Stanislas M, Laval JP, Srinath S, Soria J, Amili O, Atkinson C, Kähler CJ, Scharnowski S, Hain R, Schröder A, Geisler R, Agocs J, and Röse A (2018) Experimental evidence of near-wall reverse flow events in a zero pressure gradient turbulent boundary layer. *Exp Thermal and Fluid Science* 91:320 – 328